



Premature degradation study of a cathode-supported solid oxide electrolysis cell

Aziz Nechache¹ · Bernard A. Boukamp^{2,3} · Michel Cassir^{1,3} · Armelle Ringuedé^{1,3}

Received: 18 July 2018 / Revised: 23 September 2018 / Accepted: 24 September 2018 / Published online: 4 October 2018
© Springer-Verlag GmbH Germany, part of Springer Nature 2018

Abstract

Degradation-related issues are among the main limitations to make solid oxide electrolysis cells (SOEC) meet performance targets economically viable for long-term operation. In this study, the considered cell presents a premature degradation during electrolysis operation observed after sealing the cell holder and the support pieces providing and releasing H₂ electrode gas. This premature degradation is characterized by unusual polarization curve slopes, and appearance of a new impedance contribution at the lowest frequencies of the impedance diagrams recorded. To the best of our knowledge, this new contribution has never been reported for SOECs. *Post-mortem* analysis of the cell by scanning electron microscopy (SEM)/energy dispersive X-ray (EDX) shows the presence of Si, Al, Na, K, and Ca at the H₂ electrode interface (surface and first dozens microns in the volume) and at the Ni-yttria-stabilized zirconia (YSZ)/YSZ interface, contrary to similar cells tested before sealing the pieces. This degradation is related to Si deposition, notably at the Ni/YSZ/H₂O triple phase boundaries. Concomitantly, the new contribution observed, leading to a beneficial effect on the cell functioning, is assimilated to a “reactivation” contribution. This reactivation contribution is associated with an H₂O adsorption phenomenon and characterized by a relaxation frequency of [1–10 mHz] and a capacitance of ~ 100 F cm⁻². The evolution with time of the resistive and capacitive contributions is consistent with the interpretation of the premature cell degradation. A mechanism explaining the cell behavior after this premature degradation is proposed.

Keywords Hydrogen · Solid oxide electrolysis cell · Electrochemical impedance spectroscopy · Degradation · Si impurities · Reaction mechanisms

Introduction

Energy production through renewable sources is a critical challenge for the twenty-first century. The main route for producing energy is still nowadays based on fossil fuels, which are

expected to significantly decrease in a few decades. It is hence crucial to rethink our approach by (i) diversifying energy sources; (ii) optimizing natural energy sources such as wind, sun light, or biomass; and (iii) avoiding as much as possible pollutant and greenhouse gas generation to prevent severe environmental issues, among others, global warming. Thus, the concept of a multi-source energy production, clean and renewable, is being considered. Hydrogen production through water high temperature electrolysis (HTE) meets the conditions to be part of this concept [1–3]. Solid oxide electrolysis cells (SOEC) can be used to perform HTE. Even though significant studies appeared during the 1970s [4–7], interest on SOEC really rose during the 1980s through projects and investigations such as the Westinghouse project [8, 9], the work of Barbi and Mari [10–14], or the HOTELLY project reported by Dönitz et al. [15–18]. However, cell degradation occurring during electrolysis still represents nowadays a critical issue to make SOEC meet performance targets economically viable for possible applications, especially the ones with long-term operations. Hence, a deeper understanding of SOEC functioning and

Electronic supplementary material The online version of this article (<https://doi.org/10.1007/s10008-018-4116-7>) contains supplementary material, which is available to authorized users.

✉ Aziz Nechache
aziz.nechache@chimie-paristech.fr

✉ Armelle Ringuedé
armelle.ringuede@chimie-paristech.psl.eu

¹ PSL Research University – Chimie-ParisTech – CNRS, Institut de Recherche de Chimie Paris, 75005 Paris, France

² Department of Science and Technology & MESA Institute for Nanotechnology, University of Twente, P.O. Box 217, 7500 AE Enschede, The Netherlands

³ ISE, Chemin de Closelet 2, CH-1006 Lausanne, Switzerland

degradation is needed. In addition to post-test characterization methods such as scanning electron microscopy (SEM), X-ray diffraction (XRD), or X-ray photoelectron spectroscopy (XPS), electrochemical impedance spectroscopy (EIS) is an in situ method that is very helpful for understanding cell degradation mechanisms.

Cell degradation often occurs consequently to apparition of impurities originating from glass sealing. Chen et al. observed a severe degradation effect of volatile boron species from borosilicate glass sealant on the electrochemical activity of LSM oxygen electrode [19]. Indeed, applying 0.2 A cm^{-2} for 2 h at $T=800 \text{ }^\circ\text{C}$ led to a significant increase in both polarization and ohmic resistances. This was furthermore characterized by Sr segregation as well as boron deposition at the LSM/YSZ interface, leading to formation of lanthanum borates and manganese oxide. Consequently, disintegration and delamination of LSM electrode was accelerated by the boron deposition. Hauch et al. tested several locally produced SOFCs in HTE mode for up to 766 h [20]. The cells mainly degraded during the first 100 h of electrolysis and could be partly reactivated. In terms of EIS, degradation and activation of the cell were respectively characterized by an increase and a decrease in the polarization resistance (R_p), while the ohmic resistance (R_s) remained constant during the entire test. Based on the observation of silica containing impurities and on the work done by Jensen et al. [21], Hauch et al. suggested that (i) degradation of the cell might be due to a build-up of glassy phase impurities at the triple phase boundary (TPB) of the H_2 electrode leading to an increase in the diffusion path length at the TPB, and (ii) its partial activation could be explained by a break-up of the glass leading to a decrease in the diffusion path length at the TPB. Another study by Hauch et al. strengthened these suggestions [22]. Indeed, SOE cells tested for 1000 h were found to degrade because of silica impurities segregation at the Ni-yttria-stabilized zirconia (YSZ)/YSZ interface characterized by R_s and/or R_p increase. Silica impurities observed by SEM are supposed to segregate from glass sealing. In an additional study [23], Hauch et al. verified, by changing the type of sealing, that silica impurities segregate from the applied glass sealing to the H_2 electrode/electrolyte interface. Besides, they showed that degradation of the cell was characterized by an increase in the resistance at higher frequency part of the impedance diagram assigned here to charge transfer at the H_2 electrode [24, 25]. Ebbesen et al. examined a cell degradation for more than 1300 h in both H_2O electrolysis and $\text{H}_2\text{O}/\text{CO}_2$ co-electrolysis modes [26]. In this case, impurities originated from inlet gases. Indeed, when inlet gases were used as received, degradation of the cell occurred at both short and long term. This degradation was characterized by an increase in R_p . The use of analysis of the difference in impedance spectra (ADIS)

method allowed identifying two contributions to this degradation: one at the Ni-YSZ electrode characterized by a relaxation frequency in the 100–200 Hz range and one occurring either at the Ni-YSZ or Sr-doped LaMnO_3 (LSM)-YSZ electrodes characterized by a relaxation frequency in the 1000–3000 Hz range. Cleaning the inlet gases leads to the disappearance of the former contribution, meaning that this contribution is surely caused by impurities adsorption at the Ni-YSZ/YSZ interface, similar to what mentioned above [21–23]. Besides cell poisoning, electrolysis operation under high currents applied (above -1.0 A cm^{-2}), delamination issues at the O_2 electrode, or carbon formation at Ni-based electrodes represent other sources of detrimental degradation for SOECs [3, 27–42].

The present study deals with an early degradation phenomenon appearing after less than 200 h of test under electrolysis conditions and is attributed to cell contamination by Si impurities. We herein discuss the appearance and the evolution with time of this premature degradation based on the analysis of the EIS measurements, the post-test characterizations, and literature data. We strongly believe that this “electrochemical” approach is compulsory for understanding new kind of degradation phenomena in SOECs and optimizing the experimental conditions, which are a key step in all these high temperature devices operating with varied materials and gases.

Experimental

In this study, a LSCF//YSZ//Ni-YSZ commercial anode-supported SOFC used in HTE mode (HC Starck) was considered in a two-electrode experimental set-up. An intermediate YDC (yttria-doped Ceria) layer is present between LSCF ($\text{La}_{0.6}\text{Sr}_{0.4}\text{Co}_{0.2}\text{Fe}_{0.8}\text{O}_{3-\delta}$) and YSZ. Several H_2 leakage problems were encountered in the cathode compartment during the test bench validation process. In order to avoid such issues, the cell holder and the support pieces (alumina) used to provide and release H_2 electrode gas were sealed using Schott 8422 glass (composed of 69.8% SiO_2 , 12.0% Na_2O , 7.8% B_2O_3 , 4.1% K_2O , 0.4% CaO , and 0.2% BaO) typically used for alumina sealing, as shown in Fig. 1. The sealing was realized by increasing the temperature to $900 \text{ }^\circ\text{C}$ at $0.5 \text{ }^\circ\text{C}/\text{min}$ in flowing N_2 . This temperature was maintained for 90 min. The system was further stabilized to the operating temperature of $850 \text{ }^\circ\text{C}$ at $0.5 \text{ }^\circ\text{C}/\text{min}$. At the end of the test, the system was cooled down to room temperature at $0.5 \text{ }^\circ\text{C}/\text{min}$. Additional details of the cell and the experimental set-up are given and justified elsewhere [43]. A scanning electron microscopy (SEM) cross section image of the different layers of the cell before the test is shown in Fig. 2. The cell was tested at $850 \text{ }^\circ\text{C}$ with $\text{PH}_2\text{O}/\text{PH}_2 = 9$ at the cathode side, air at the anode side, and a gas flow rate of 2.26 NL/h at each side. The circular cell has an active electrode area of

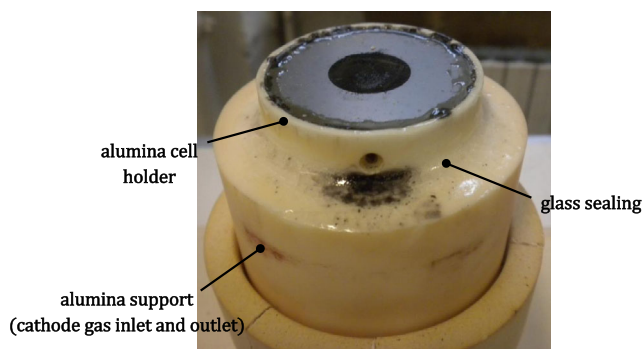
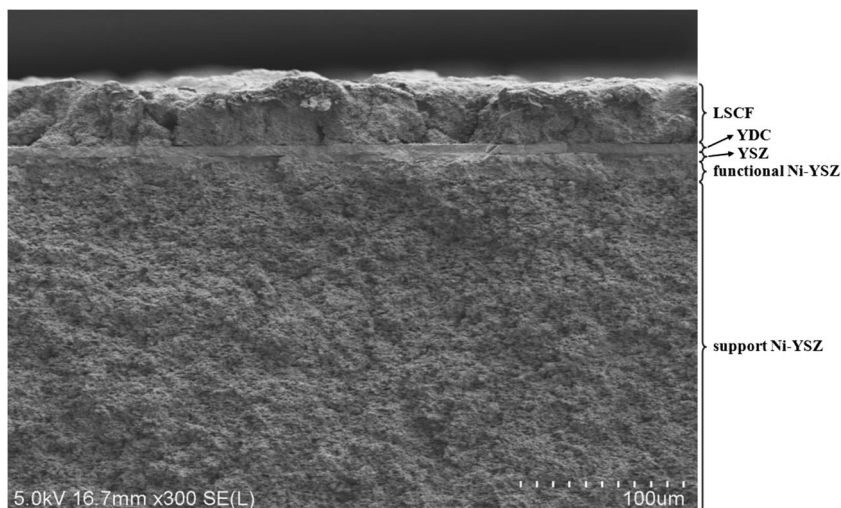


Fig. 1 Image of the cell after functioning on the alumina cell holder. The alumina support allows supplying and releasing of the cathode gas. The Schott 8422 glass sealing in between the two alumina pieces allows avoiding gas leakage at the cathode compartment

3.14 cm^2 , referring to the LSCF diameter (20 mm). A succession of impedance diagrams were measured, preceded and followed by current density-potential (i - U) curves. The overall 8-h procedure was repeated with time. Thus, to study the appearance and the evolution with time of the premature degradation, the cell is analyzed initially (0 h), after 144 h and after 168 h of working time. The i - U curves were recorded in potentiostatic mode with a scan rate of 1 mV/s . The electrochemical impedance diagrams were recorded applying a dc current with a 30 mA amplitude perturbation in the frequency range from 10 to 0.01 Hz with 10 points per decade. A Biologic SP-150 frequency analyzer with a 20 A booster was used for both chronopotentiometry and EIS measurements. Post-mortem analyses of the tested cell were performed using a Hitachi SU-70 SEM-FEG equipped with an Oxford X-Max 50 mm^2 X-ray microanalysis system for the energy dispersive X-ray (EDX) spectroscopy (detection limit, $1.0 \text{ wt}\%$). In our case, analyses were carried out with an acceleration voltage of 15 kV . No additional coating was required to clearly observe by SEM the surfaces and the considered layers.

Fig. 2 SEM cross section image of the different layers constituting the cell before the test, as follows from bottom to top: Ni-YSZ electrode supporting layer, Ni-YSZ electrode functional layer, YSZ electrolyte, YDC intermediary layer, and LSCF electrode



Results and discussions on electrochemical measurements

Premature degradation appearance

In a similar study recently reported [43], the i - U curve measured showed three functioning regions (curve at 0 h in Fig. 3): region I where R_p decreases with increasing current densities corresponding to a decrease in the activation resistance, region II where R_p reaches a minimum and remains constant while current density increases showing an optimal use of the cell, and region III where R_p increases with current density resulting mainly from an increase in concentration overpotentials. According to Fig. 3, the i - U curve measured in this study (at $t = 144 \text{ h}$) shows a particular trend: five functioning regions can be distinguished instead of three, which leads to a “double basin-like” evolution of the total resistance (R_t) with current density, as shown in Fig. 4a. Indeed, after a decrease in R_t during cell activation (region I), the “optimal cell utilization” region appears at -0.2 A cm^{-2} (region II). From -0.3 to -0.6 A cm^{-2} R_t increases again, indicating that the cell is already working under gas transport limitation (region III) before decreasing again to reach a minimum value of $0.41 \Omega \text{ cm}^2$ at -0.8 A cm^{-2} (region IV). Note that R_t at -0.8 A cm^{-2} is smaller than the $0.54 \Omega \text{ cm}^2$ obtained at -0.2 A cm^{-2} . Finally, R_t increases to reach $1.41 \Omega \text{ cm}^2$ at -1.05 A cm^{-2} (region V). The degradation thus leads to a perturbation in cell operation from the very first current densities applied.

According to the orders of magnitude for R_p and R_s as well as their variations with current density (Fig. 4a, b, respectively), the “double basin-like” evolution of R_t with current density is imposed by R_p variations. Thus, the cell behavior mainly depends on the reaction processes included in the polarization resistance. Nevertheless, the ohmic resistance tends to increase until -0.4 A cm^{-2} (13% increase) to further decrease

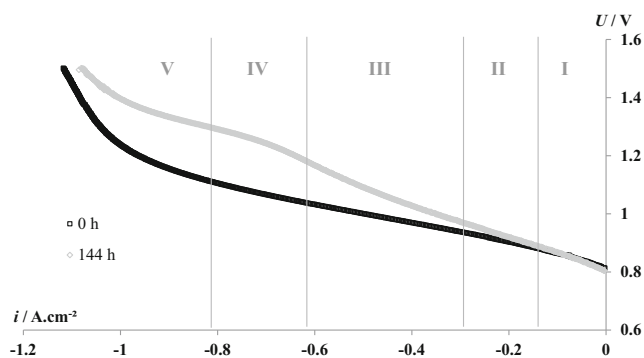


Fig. 3 Polarization curve (i - U curve) of the cell after (\square) 0 h and (\diamond) 144 h of test. The i - U curve measured after 144 h of test shows five functioning regions: region I corresponding to a decrease in the activation resistance, region II to an optimal use of the cell, region III resulting mainly from an increase of concentration overpotentials, region IV corresponding to the cell reactivation until limitation by H_2O transport becomes the predominant phenomenon governing the cell functioning (region V). $T = 850$ °C, $PH_2O/PH_2 = 9$ (H_2 electrode), air (O_2 electrode), standard flow rate of 2.26 NL h^{-1} on both sides

and even reaches a value inferior to the one at open-circuit voltage (OCV) ($R_s = 0.141$ Ω cm^2 at $i = 0$ A cm^{-2} whereas $R_s = 0.135$ Ω cm^2 at $i = -1.05$ A cm^{-2}). This transition

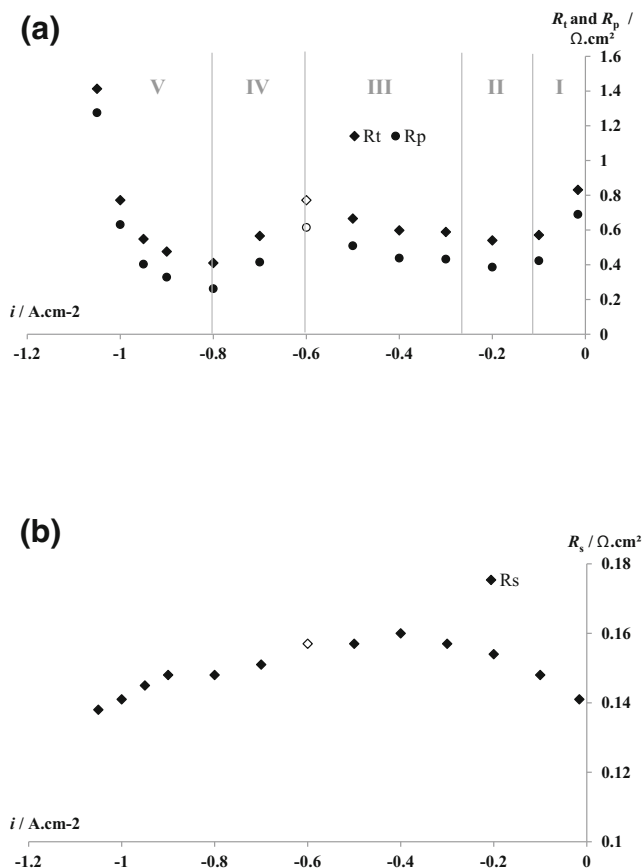


Fig. 4 Total and polarization resistances R_t and R_p (a), ohmic resistance R_s of the cell after 144 h of test (b). $T = 850$ °C, $PH_2O/PH_2 = 9$ (H_2 electrode), air (O_2 electrode), standard flow rate of 2.26 NL h^{-1} on both sides. The unfilled points correspond to the appearance of region IV. R_p values were measured as explained in [Appendix A](#)

happens for a cell voltage superior to 1.1 V, which is consistent with an endo/exothermic transition. Details on the measurement method of R_p values are given in [Appendix A](#).

The impedance diagrams recorded in the five regions and shown in [Fig. 5](#) lead to the following qualitative analysis:

- Region I: R_p decreases during the activation of the cell at the first current densities applied. This is characterized by a slight decrease in the high frequency (HF) part of the impedance diagram, and a more important decrease in the middle frequency (MF) and low frequency (LF) parts ([Fig. 5a](#)).
- Region II: [Figure 5b](#) shows that the optimal utilization region is severely shortened compared to our previous study in which the cell holder and support pieces were not sealed [43]. Indeed, a slight increase of R_p is observed between -0.2 and -0.4 A cm^{-2} . This is characterized by (i) an important increase in the HF part associated with charge transfer at the Ni-YSZ/electrolyte interface [43–47]; (ii) a slight decrease in the MF part that maybe related to H_2O transport phenomena at the Ni-YSZ electrode [43, 45, 48–50]; and (iii) a slight decrease in the LF part attributed to H_2O diffusion at the Ni-YSZ electrode [44, 51–54]. This indicates that the cell starts being disturbed by a phenomenon affecting mainly H_2 electrode interfacial charge transfer at this stage.
- Region III: R_p still increases between -0.4 and -0.6 A cm^{-2} ([Fig. 5c](#)) with an even more important increase of the HF part, but also this time an important increase in the MF and LF parts of the diagram. This indicates that, in addition to interfacial charge transfer, this phenomenon now affects H_2O transport at the H_2 electrode, explaining the early appearance of gas transport limitation on the i - U curve ([Figs. 3](#) and [4a](#)).
- Region IV: Above -0.6 A cm^{-2} ([Fig. 5c](#)), the appearance of region IV corresponds to a decrease in R_p characterized by two contradictory trends. On the one hand, the overall impedance diagram increases until a certain frequency (0.1 Hz for $i = -0.8$ A cm^{-2}) and, on the other hand, a positive contribution, which is akin to a “reactivation” of the cell, appears and leads to a decrease in the impedance diagram at the lowest frequencies, which explains the decrease in R_p . It should be noticed that, according to the R_t (and so R_p) value, this reactivation contribution is significantly more important than what is observed from the impedance diagram only recorded until 0.01 Hz.
- Region V: Located above -0.8 A cm^{-2} , region V is characterized by the same trends as region IV, the transition happening for lower frequencies as the current density applied increases ([Fig. 5d](#)). Hence, considering that region III corresponds to gas transport limitation, the appearance of the reactivation contribution counterbalances gas transport limitation (region IV) up to a certain current

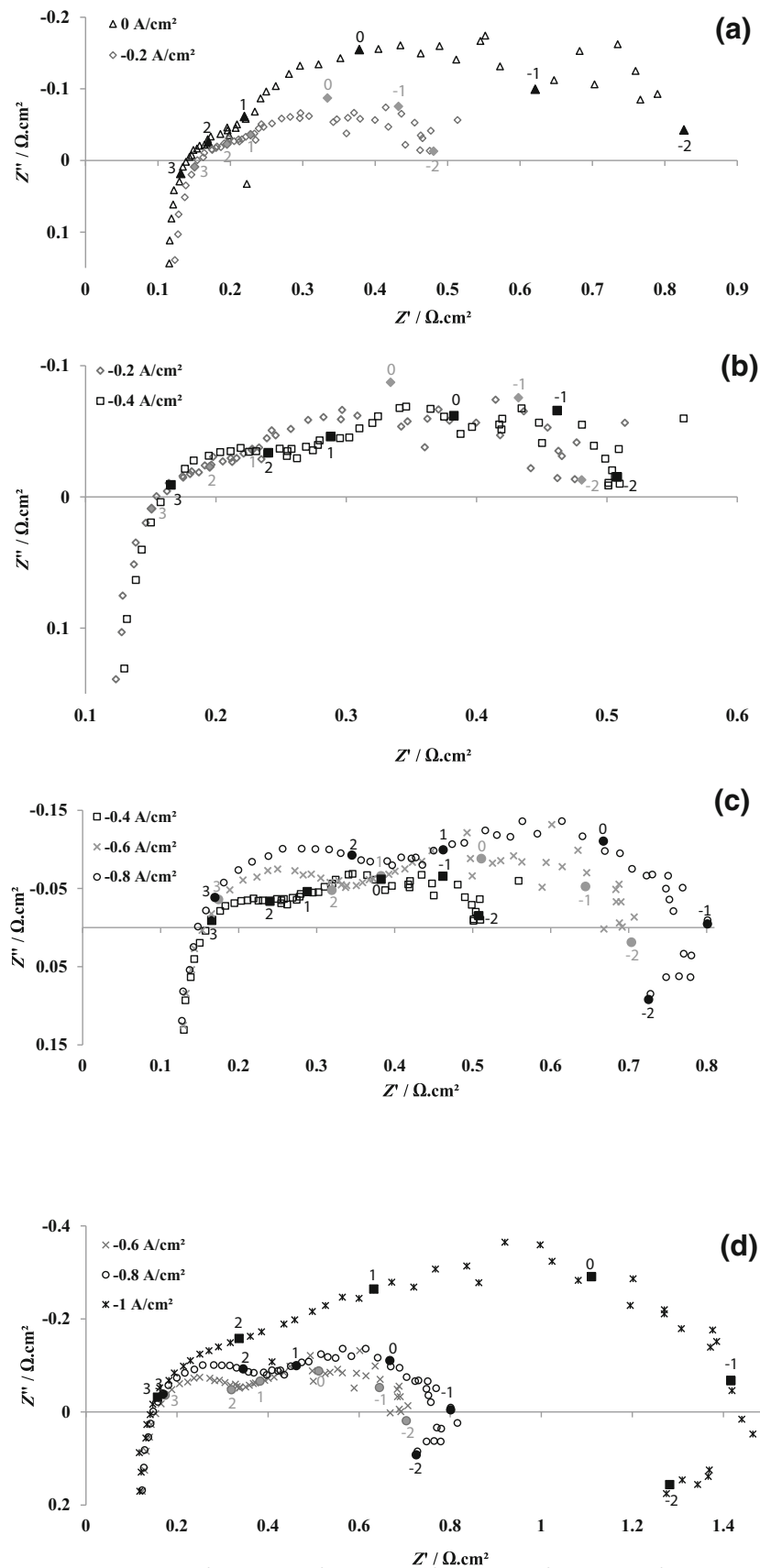


Fig. 5 a–d Impedance diagrams recorded at $0 A cm^{-2}$, $-0.2 A cm^{-2}$, $-0.4 A cm^{-2}$, $-0.6 A cm^{-2}$, $-0.8 A cm^{-2}$, and $-1.0 A cm^{-2}$ after 144 h of test. $T = 850 ^\circ C$, $PH_2O/PH_2 = 9$ (H_2 electrode), air (O_2 electrode), standard flow rate of $2.26 NL h^{-1}$ on both sides

Table 1 Values of relaxation frequency f_0 and capacitance C obtained after fitting of the impedance diagrams shown in Fig. 5 using the electrical equivalent circuit in Fig. 6a for $i = 0, -0.2, -0.4$, and -0.6 A cm^{-2} , while the one in Fig. 6b was used for $i = -0.8$ and -1.0 A cm^{-2}

	f_{HF} (Hz)	f_{MF1} (Hz)	f_{MF2} (Hz)	f_{LF} (Hz)	f_{VLF} (Hz)	C_{HF} (F/cm ²)	C_{MF1} (F/cm ²)	C_{MF2} (F/cm ²)	C_{LF} (F/cm ²)	C_{VLF} (F/cm ²)
0 A/cm ²	405	18	1.16	0.091	–	0.020	0.502	1.72	16.0	–
–0.2 A/cm ²	815	66	2.29	0.178	–	0.012	0.195	1.66	22.9	–
–0.4 A/cm ²	703	32	1.77	0.116	–	0.008	0.198	2.48	41.5	–
–0.6 A/cm ²	499	14	1.50	0.134	–	0.005	0.342	2.19	28.3	–
–0.8 A/cm ²	371	17	1.89	0.176	0.004	0.006	0.214	1.11	28.9	–341
–1.0 A/cm ²	234	20	2.04	0.209	0.007	0.008	0.085	0.37	12.3	–114

It should be noted that the statistical errors for the impedance spectra fitting results did not exceed 8.4%

density value above which transport limitation prevails over the other reaction phenomena, including the one related to the reactivation contribution (region V).

Table 1 contains relaxation frequency f_0 and capacitance C values obtained by deconvolution of the impedance diagrams shown in Fig. 5. Up to $i = -0.6 \text{ A cm}^{-2}$, the equivalent electrical circuit shown in Fig. 6a was used; it is composed of an ohmic resistance R_s (corresponding to R_{Ω}) in series with an inductance L and four combinations of a resistance R in parallel with a constant phase element CPE ($R//CPE$). For $i = -0.8$ and -1.0 A cm^{-2} , a fifth $R//CPE$ was required (Fig. 6b). This fifth element allows taking into account the reactivation contribution, firstly assigned to an inductive contribution, but finally modeled with a differential negative resistance in parallel with a differential negative capacitance (pseudo-capacitive negative behavior). Having a negative resistance is relevant with the beneficial effect of this reactivation contribution on the cell functioning. Further discussions involving these two negative elements will be based on the absolute values obtained from the fitting.

Table 1 clearly shows that, depending on the current density considered, four to five main phenomena can be distinguished, each phenomenon characterized by a specific

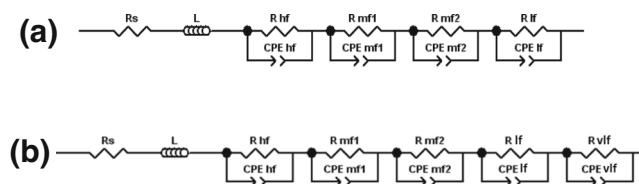


Fig. 6 Electrical equivalent circuits used to fit the impedance diagrams from Fig. 5. **a** Up to $i = -0.6 \text{ A cm}^{-2}$, an equivalent electrical circuit composed of a ohmic resistance R_s (corresponding to R_{Ω}) in series with an inductance L and four combinations of a resistance R in parallel with a constant phase element CPE ($R//CPE$) was used. **b** For $i = -0.8$ and -1.0 A cm^{-2} , a fifth $R//CPE$ was required. R_{HF} and CPE_{HF} are associated with charge transfer at the Ni-YSZ/YSZ interface, R_{MF1} and CPE_{MF1} with H_2O diffusion at the Ni-YSZ electrode, R_{MF2} and CPE_{MF2} with H_2O gas conversion at the Ni-YSZ electrode, while R_{LF} and CPE_{LF} are also associated with H_2O diffusion at the Ni-YSZ electrode. R_{VLF} and CPE_{VLF} are related to the new reactivation contribution

relaxation frequency and capacitance. Thus, there are four to five main phenomena governing the cell operation in this study.

The four to five frequency ranges identified after deconvolution of the impedance diagrams are designated as HF, MF1, MF2, LF, and VLF (for very low frequency) arcs, from high to low frequencies. Except for the VLF arc, the four other orders of magnitude correspond to those obtained in a previous study [43]: $\{[100-1000 \text{ Hz}], 10 \text{ mF cm}^{-2}\}$, $\{10 \text{ Hz}, 0.1 \text{ F cm}^{-2}\}$, $\{1 \text{ Hz}, 1 \text{ F cm}^{-2}\}$, and $\{0.1 \text{ Hz}, 10 \text{ F cm}^{-2}\}$, respectively. The main difference in the present study is the sealing of the two alumina pieces that provide and release H_2 electrode gas. Consequently, any change in the identified phenomena would mean that these are associated with the cathode side of the electrolyzer.

The first analysis of the impedance diagrams shows that, depending on the current density considered, all or part of the diagram is influenced by the appearance of the reactivation contribution. This allows us pointing out the following statements:

(i) This confirms that HF, MF2, and LF arcs are respectively associated with charge transfer at the Ni-YSZ/YSZ interface, H_2O gas conversion at the Ni-YSZ electrode, and H_2O diffusion at the Ni-YSZ electrode.

(ii) It also proves that the MF1 arc is also related to a cathode phenomenon. The influence of $\text{PH}_2\text{O}/\text{PH}_2$ ratio and cathode gas flow rate on the MF1 arc was highlighted elsewhere [43, 45, 48]. This allows to relate MF1 arc to a phenomenon associated with H_2O transport at the Ni-YSZ electrode. Besides, the influence of $\text{H}_2\text{O}/\text{H}_2$ dilution with N_2 on MF1 arc suggests its association with H_2O diffusion on the cathode side [43]. This association is now confirmed as well; the MF1 arc is related to H_2O diffusion at the Ni-YSZ electrode.

It is also important to underline that the new reactivation contribution is clearly distinguishable from the other contributions with orders of magnitude of $[1-10 \text{ mHz}]$ for the relaxation frequency and $[100 \text{ F cm}^{-2}]$ for the capacitance.

The reactivation contribution is characterized by the appearance of the negative differential resistance at the lowest frequencies R_{VLF} , which absolute value increases with current

density (Table B1, Appendix B). Thus, as shown in Table 2, the appearance of this reactivation contribution improves the cell operation ($|R_{VLF}|/R_{MF1} = 2.9$ and $|R_{VLF}|/R_{LF} = 4.0$), before H₂O transport phenomena becomes dominant as shown by the decrease in the ratios $|R_{VLF}|/R_{MF1}$ (from 2.9 to 2.3), $|R_{VLF}|/R_{MF2}$ (from 1.7 to 1.0), and $|R_{VLF}|/R_{LF}$ (from 4.0 to 3.4). Details of the resistance values obtained by fitting are shown in Table B1.

Premature degradation evolution with time

To understand the evolution of R_p with time, a qualitative analysis of the impedance diagrams recorded at the most relevant current densities applied was realized, leading to the following observations:

- At OCV (Fig. 7a), an increase with time in the whole impedance diagram is observed, even if the lower frequency part becomes more difficult to observe with time because of the instability of the cell.
- When $i = -0.2 \text{ A cm}^{-2}$ is applied (Fig. 7b), the cell already reaches the “pseudo” optimal utilization region at 144 h and 168 h, while the system is still activating at 0 h. However, from 0 to 144 h, the whole impedance diagram increases as well, whereas from 144 to 168 h, it is the HF part of the diagram which mainly increases. This means that from the first current densities applied, all the main phenomena dominating the cell functioning, especially charge transfer at the Ni-YSZ/YSZ interface and the different phenomena related to H₂O transport at the Ni-YSZ electrode, are disrupted, up to a certain time above which interfacial charge transfer is mainly disrupted.
- When $i = -0.4 \text{ A cm}^{-2}$ (Fig. 7c) is applied, the cell reaches the optimal utilization region at 0 h while it is already in the H₂O transport limitation region at 144 h and 168 h. This is once again characterized by an increase in the whole impedance diagram from 0 to 144 h, but also from 144 to 168 h. Thus, at this functioning state of the cell, all the dominating phenomena are affected, whatever the time considered.
- From $i = -0.6 \text{ A cm}^{-2}$ (Fig. 7d) to $i = -0.8 \text{ A cm}^{-2}$ (Fig. 7e) applied, the cell is in the region IV of reactivation for 144 h and 168 h while it only starts reaching the H₂O transport limitation region at 0 h. In this case, the whole impedance diagram still increases with time but the reactivation contribution appears at the lowest frequencies for

144 h and 168 h, and this from -0.6 A cm^{-2} for 168 h. Thus, even if the main phenomena dominating the cell are still disrupted, appearance of the reactivation contribution allows the renewal of the cell performance, and this for a lower value of current density applied with time. H₂O transport limitation is, at this stage, counterbalanced by the reactivation contribution.

- Above -0.8 A cm^{-2} applied, the current demand of the cell is so large that the system is reaching a region where H₂O transport limitation predominates the functioning of the cell, whatever the time considered. This is characterized notably at -1.0 A cm^{-2} (Fig. 7f) by an increase in the whole impedance diagram.

It is important to notice that the R_p value evolves differently with time depending on the current density applied. Indeed, until -0.5 A cm^{-2} , R_p increases with time. However, above -0.5 A cm^{-2} applied, this trend is reversing progressively until -0.8 A cm^{-2} , value from which R_p decreases with time. This trend is in accordance with the interpretation made previously regarding the appearance of the premature degradation.

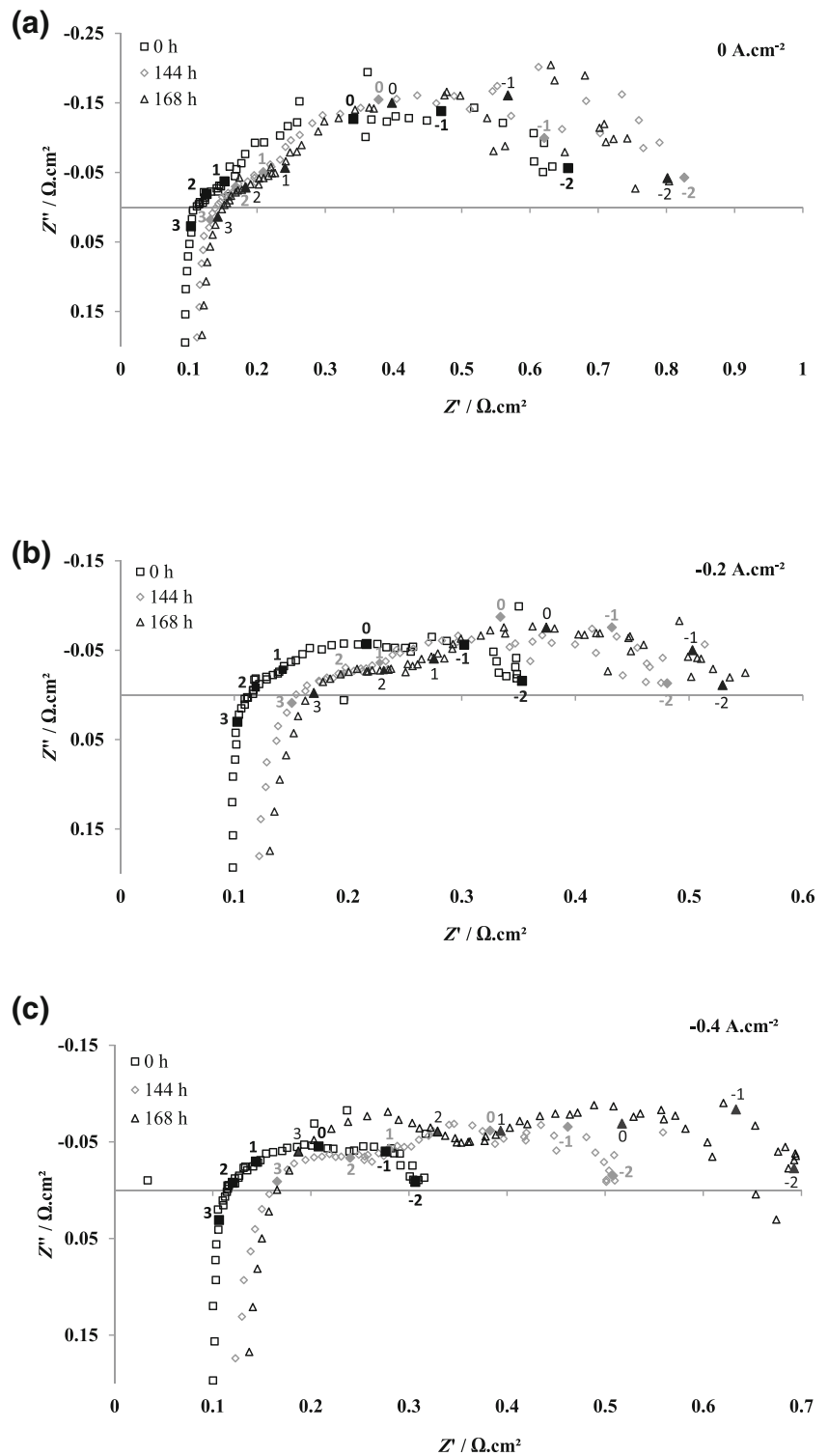
According to Table C1 (cf. Appendix C), f_0 and C values obtained from the fittings using the electrical equivalent circuits shown Fig. C1 (cf. Appendix C) allow distinguishing the same four to five main phenomena for the functioning of the cell as the ones obtained earlier. However, more or less important shifts of f_0 and C can be noticed with time and current density change, and make this distinction less obvious. Nevertheless, this distinction remains clear when one duration is considered.

Table 3 shows the ratios $R_{144 \text{ h}}/R_{0 \text{ h}}$ and $R_{168 \text{ h}}/R_{144 \text{ h}}$ for the frequency ranges HF, MF1, MF2, LF, and VLF at the different current densities of the impedance diagrams presented in Fig. 7. Most of these ratios are above 1.0, which means an increase with time in the resistance for all the contributions. It should be however noted that for the LF part, the ratio $R_{168 \text{ h}}/R_{144 \text{ h}}$ varies between 0.72 and 1.0, whereas $R_{144 \text{ h}}/R_{0 \text{ h}}$ is mostly above 1.0. Thus, contrary to the other phenomena, the H₂O diffusion phenomenon at the Ni-YSZ electrode associated with the LF part tends to be less resistive with time. This is related to the appearance of the reactivation contribution. Indeed, at 144 h, when this new contribution appears, the LF part is still present while at 168 h, it is not anymore. It is moreover interesting to notice that when the ratios $R_{144 \text{ h}}/R_{0 \text{ h}}$ and $R_{168 \text{ h}}/R_{144 \text{ h}}$

Table 2 $|R_{VLF}|/R_X$ ratios between VLF part and the four other frequency ranges HF, MF1, MF2, and LF, for -0.8 A cm^{-2} and -1.0 A cm^{-2}

	$ R_{VLF} / R_{HF}$	$ R_{VLF} / R_{MF1}$	$ R_{VLF} / R_{MF2}$	$ R_{VLF} / R_{LF}$
-0.8 A/cm^2	1.7	2.9	1.7	4.0
-1.0 A/cm^2	2.6	2.3	1.0	3.4

Fig. 7 Impedance diagrams recorded at 0 A cm^{-2} (a), -0.2 A cm^{-2} (b), -0.4 A cm^{-2} (c), -0.6 A cm^{-2} (d), -0.8 A cm^{-2} (e), and -1.0 A cm^{-2} (f) after $t = (\square)$ 0 h, (\diamond) 144 h, and (\triangle) 168 h of test. $T = 850 \text{ }^\circ\text{C}$, $P_{\text{H}_2\text{O}}/P_{\text{H}_2} = 9$ (cathode), air (anode), gas flow rate of 2.26 NL h^{-1} on both sides



are considered, the values are particularly high for the HF and MF1 parts. Indeed, according to Table 3, for the HF part, $R_{144 \text{ h}}/R_{0 \text{ h}}$ and $R_{168 \text{ h}}/R_{144 \text{ h}}$ ratios reach up to 8.5 and 2.5, respectively, and, for the MF1 part, 3.9 and 2.3, respectively. On the contrary, except the values at 0 A/cm^2 ,

these ratios are mostly inferior to 2 for the MF2 and LF parts. Thereby, the phenomena related to the HF and MF1 parts are the most affected by the degradation with time, the one related to the HF part being especially affected initially according to the ratio $R_{144 \text{ h}}/R_{0 \text{ h}}$.

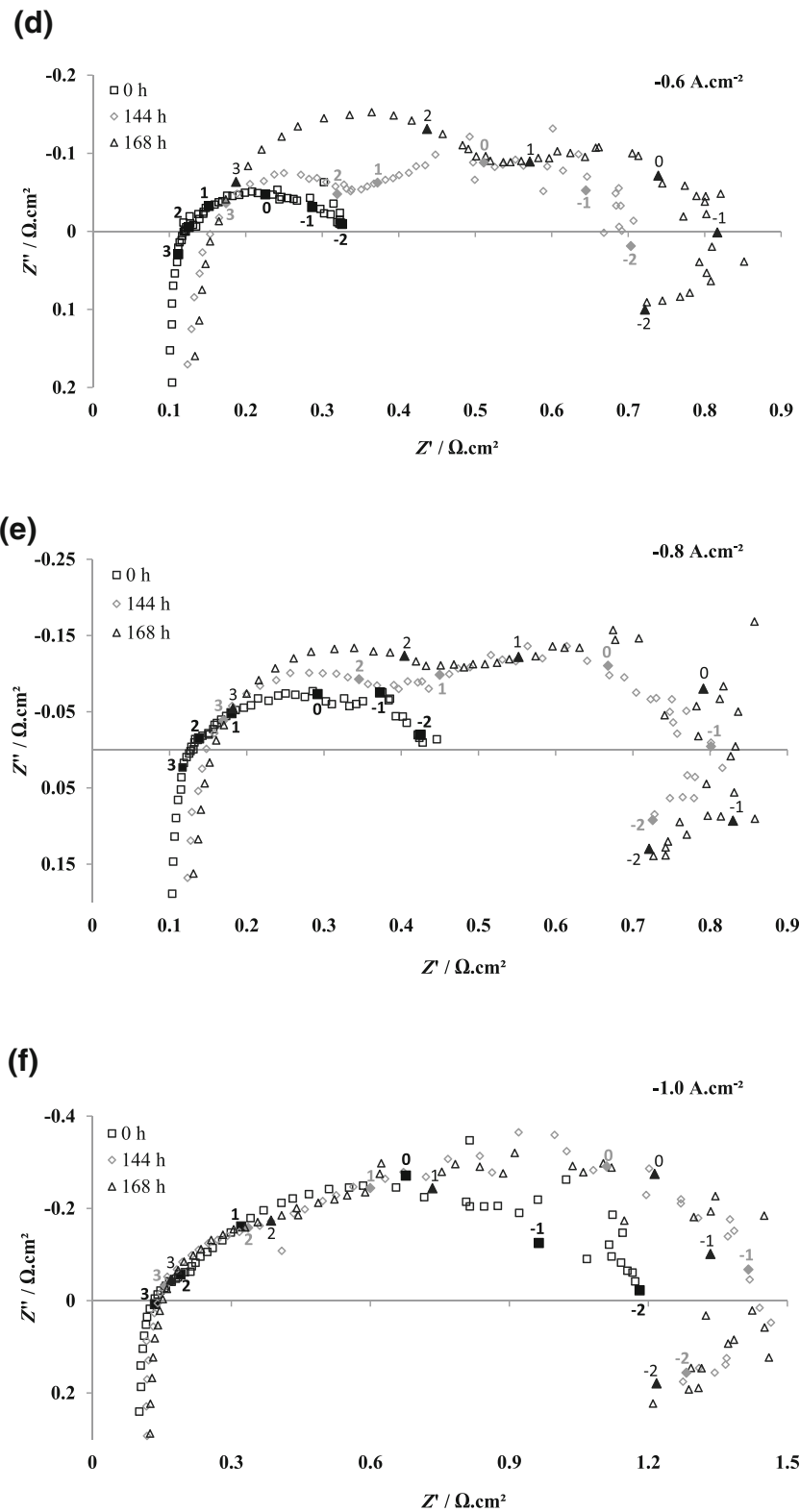


Fig. 7 continued.

Table 4 shows the ratios $C_{144 \text{ h}}/C_{0 \text{ h}}$ and $C_{168 \text{ h}}/C_{144 \text{ h}}$ for the HF, MF1, MF2, LF, and VLF parts at different current densities. The ratio $C_{144 \text{ h}}/C_{0 \text{ h}}$ is systematically inferior to

1.0, which means that all the capacitances related to the main phenomena decrease with time. This decrease is particularly important for the HF and MF1 parts which ratios are mostly

Table 3 $R_{144\text{ h}}/R_{0\text{ h}}$ and $R_{168\text{ h}}/R_{144\text{ h}}$ ratios for the frequency ranges HF, MF1, MF2, LF, and VLF for different current densities, including the ones of the impedance diagrams shown in Fig. 7

$R_{144\text{ h}}/R_{0\text{ h}}$	HF	MF1	MF2	LF	VLF
0 A cm ⁻²	2.1	1.8	2.6	3.2	–
–0.2 A cm ⁻²	2.1	1.4	1.6	1.3	–
–0.4 A cm ⁻²	4.1	2.9	1.5	1.2	–
–0.5 A cm ⁻²	5.0	3.9	1.6	1.4	–
–0.6 A cm ⁻²	8.5	3.3	1.5	2.1	–
–0.8 A cm ⁻²	6.2	2.7	1.3	1.5	–
–1.0 A cm ⁻²	3.6	1.2	1.5	0.68	–
–1.05 A cm ⁻²	1.8	0.84	1.1	0.75	–
$R_{168\text{ h}}/R_{144\text{ h}}$	HF	MF1	MF2	LF	VLF
0 A cm ⁻²	0.92	1.3	1.2	0.76	–
–0.2 A cm ⁻²	1.9	2.3	0.92	0.72	–
–0.4 A cm ⁻²	2.2	1.5	1.1	1.0	–
–0.5 A cm ⁻²	2.5	1.7	1.3	0.81	–
–0.6 A cm ⁻²	2.0	1.4	1.2	–	–
–0.8 A cm ⁻²	1.2	1.2	1.1	–	1.3
–1.0 A cm ⁻²	1.1	1.5	0.97	–	1.7
–1.05 A cm ⁻²	1.1	1.2	1.1	–	1.6

between 0.1 and 0.2, meaning a capacitance variation with a factor from 5 to 10 between 0 and 144 h.

Thus, appearance of the premature degradation is characterized with time by a decrease in all capacitances, which is surprising since this trend is rather the sign of a favorable evolution of the cell functioning with time, while a

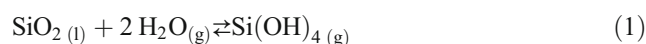
Table 4 $C_{144\text{ h}}/C_{0\text{ h}}$ and $C_{168\text{ h}}/C_{144\text{ h}}$ ratios for the frequency ranges HF, MF1, MF2, LF, and VLF for different current densities, including the ones of the impedance diagrams shown in Fig. 7

$C_{144\text{ h}}/C_{0\text{ h}}$	HF	MF1	MF2	LF	VLF
0 A cm ⁻²	0.23	0.25	0.45	0.30	–
–0.2 A cm ⁻²	0.21	0.14	0.47	0.47	–
–0.4 A cm ⁻²	0.18	0.16	0.69	0.88	–
–0.5 A cm ⁻²	0.19	0.21	0.85	0.55	–
–0.6 A cm ⁻²	0.14	0.28	0.73	0.36	–
–0.8 A cm ⁻²	0.12	0.10	0.41	0.29	–
–1.0 A cm ⁻²	0.44	0.36	0.44	0.67	–
–1.05 A cm ⁻²	0.61	0.50	0.43	0.64	–
$C_{168\text{ h}}/C_{144\text{ h}}$	HF	MF1	MF2	LF	VLF
0 A cm ⁻²	1.1	0.86	1.2	1.9	–
–0.2 A cm ⁻²	0.67	4.8	2.7	2.5	–
–0.4 A cm ⁻²	0.63	3.4	1.6	1.0	–
–0.5 A cm ⁻²	0.71	2.9	1.4	2.3	–
–0.6 A cm ⁻²	1.0	1.3	0.86	–	–
–0.8 A cm ⁻²	0.83	0.43	0.64	–	0.64
–1.0 A cm ⁻²	0.88	0.89	1.3	–	1.8
–1.05 A cm ⁻²	0.82	0.86	1.3	–	1.7

degradation of the cell is observed. On the other hand, this trend is predominantly reversed when the ratio $C_{168\text{ h}}/C_{144\text{ h}}$ is considered since most of the capacitances increase with time. In this case, the MF1, MF2, and LF parts are the most characteristic of this increase, meaning that the capacitances related to the H₂O transport phenomena are mostly increasing between 144 and 168 h. This is in accordance with a more difficult H₂O transport processing as a consequence of the premature degradation. A possible explanation might be that H₂O transport in the cell is disturbed, leading locally to the accumulation of H₂O in the porous path along the way from the surface to the Ni-YSZ/YSZ interface. With values between 0.63 and 1.1, the HF part ratios are mostly inferior to 1, meaning that the HF capacitances associated to charge transfer at the Ni-YSZ/YSZ interface are still decreasing between 144 and 168 h. This decrease is however much less important than between 0 and 144 h. This clearly shows that, with time, the premature degradation has more influence on the capacitive behavior of all the main electrochemical processes governing cell functioning, including charge transfer at the Ni-YSZ/YSZ interface. Consequently, the evolution of the degradation with time seems to be mainly shown above 144 h by an increase in most of the capacitances related to the phenomena dominating the cell functioning, except charge transfer which continues to decrease.

Discussion on the premature degradation origins

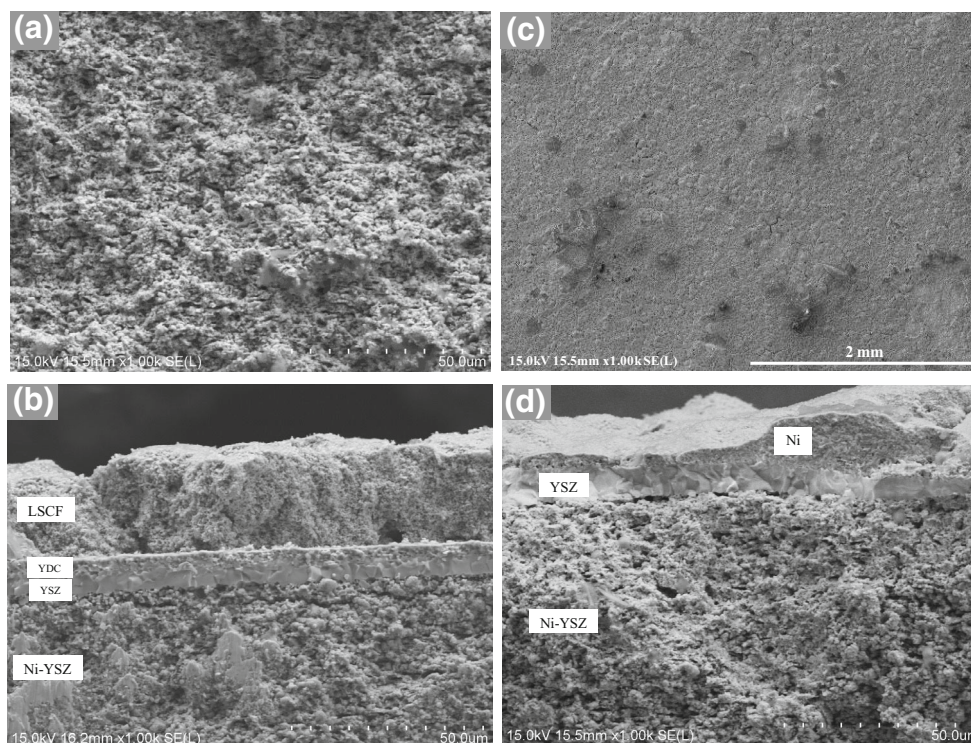
It is first worth reminding that the set-up was modified for this test by sealing the cell holder and the support pieces (see Fig. 1). The premature degradation was not observed for the tests realized before sealing the pieces, including the one discussed elsewhere [43]. Consequently, this degradation is related to the sealing done using Schott 8422 glass composed of SiO₂ (69.8%), B₂O₃ (7.8%), Na₂O (12.0%), K₂O (4.1%), CaO (0.4%), and BaO (0.2%). We know that the two pieces provide and release H₂ electrode gas composed of 90% H₂O and 10% H₂. Besides, according to Hauch et al. [22], in the experimental conditions of this test, SiO₂ and H₂O can generate gaseous Si(OH)₄ as follows:



Once deposited, Si can segregate in the volume of Ni-YSZ electrode up to the Ni-YSZ/YSZ interface, this segregation being facilitated by the presence of Na₂O and Al₂O₃ [55–61].

Figure 8 shows the post-mortem SEM images of the tested cell, with a transversal cut of the H₂ electrode volume (Fig. 8a), a transversal cut of the complete cell (Fig. 8b), the

Fig. 8 Post-mortem SEM images of the tested cell, with a transversal cut of the H₂ electrode volume (a), a transversal cut of the complete cell (b), including LSCF, YDC, and YSZ layers, and the first dozens of microns of Ni-YSZ cathode (from the Ni-YSZ/YSZ interface), the H₂ electrode surface (c), and a transversal cut of the first dozens of microns for the H₂ electrode (d) with, from the surface, a Ni layer, a dense 8YSZ layer, and the Ni-YSZ cermet. It should be noticed that the Ni layer is for current collection at the H₂ electrode surface while the dense 8YSZ layer aims at maintaining mechanically the cell [62]



H₂ electrode surface (Fig. 8c), and a transversal cut of the first dozens of microns of the H₂ electrode (Fig. 8d).

Table 5 contains the amounts of Si, Al, Na, Ka, and Ca elements obtained by SEM/EDX analyses. All the results are presented in atomic percentage.

The MEB/EDX analyses do not show any presence of Si in the H₂ electrode volume, but rather at the Ni-YSZ/YSZ interface. Besides, a regular presence of Si, Al, Na, K, and Ca is noticed at the H₂ electrode surface and at the first dozens of microns in the volume from the surface. These elements are also detected in the LSCF and YDC volumes, as for tests

anterior to the sealing of the two alumina pieces [63], meaning that this is not linked to the premature degradation of the cell. On the contrary, no trace of these elements was observed at the surface or the volume of the H₂ electrode, or at the Ni-YSZ/YSZ interface for the tests anterior to the sealing [63]. Thus, this degradation is related to the presence of Si, at the H₂ electrode surface and at low depth mainly, as well as at the Ni-YSZ/YSZ interface. There might have been formation of Si(OH)₄ from SiO₂ and H₂O as Hauch et al. suggested [22] leading in our case to Si deposit on the H₂ electrode surface and Si segregation in the first dozens of microns in the volume

Table 5 Amounts of Si, Al, Na, Ka, and Ca elements obtained by SEM/EDX analyses for the different areas and layers of the tested cell shown in Fig. 8

	Fig. 8a	Fig. 8b			Fig. 8c	Fig. 8d			
	Ni-YSZ volume	Anode LSCF	Intermediate layer YDC	Electrolyte YSZ	Cathode Ni-YSZ	Ni-YSZ surface	Ni	YSZ	Ni-YSZ
Si	0.0*/0.0	5.8* ^a /4.5	0.7* ^a /0.8	0.0*/0.0	0.0*/0.4	0.0*/3.8	0.0*/0.8	0.0*/0.0	0.0*/0.4
Al	0.2*/0.3	0.7* ^a /0.6	0.3* ^a /0.2	0.1*/0.2	0.3*/0.3	0.2*/0.5	1.0*/1.1	0.1*/0.2	0.7*/0.9
Na	0.0*/0.1	0.4* ^a /0.5	0.0* ^a /0.0	0.0*/0.0	0.1*/0.2	0.0*/0.4	0.0*/0.7	0.0*/0.1	0.0*/0.4
K	0.0*/0.0	0.4* ^a /0.4	0.0* ^a /0.0	0.0*/0.0	0.0*/0.1	0.0*/0.3	0.0*/0.4	0.0*/0.1	0.0*/0.2
Ca	0.0*/0.0	0.2* ^a /0.3	0.0* ^a /0.0	0.0*/0.0	0.0*/0.1	0.0*/0.3	0.0*/0.5	0.0*/0.2	0.0*/0.2

All the results are presented in atomic percentage

*Mean value of the amounts observed in previous studies [63]

^a Amounts due to the set-up configuration where the sealing glass is applied on the O₂ electrode side [43, 63]

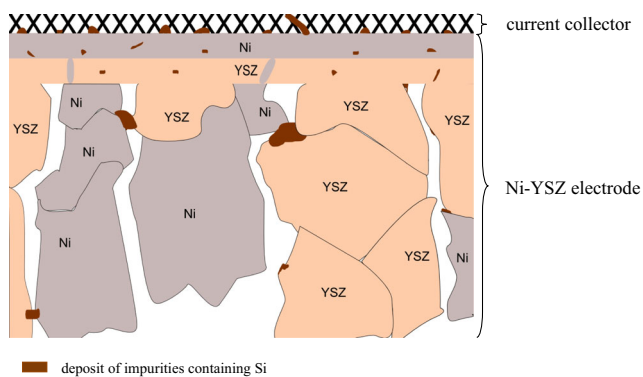


Fig. 9 Illustration of impurity deposits containing Si (brown) at the origin of the premature cell degradation. These impurities are mainly located at the Ni-YSZ electrode surface as well as the first dozens of micron in depth from the surface

from the surface, and also at the Ni-YSZ/YSZ interface. Hence, in our electrolysis conditions, the presence of Si has

an important influence on cell degradation, contrary to a study made by Virkar in SOFC mode [64].

We interpret the behavior of the cell and its premature degradation as follows. The presence of Si at the H₂ electrode surface and low depth disturbs charge transfer at the cathode side from the lowest current densities applied, because of a direct contact with the current collectors, as well as H₂O transport necessary for the reduction reaction at the Ni-YSZ/YSZ interface. Disruption of H₂O transport, which is only partial first according to the earlier discussion, becomes increasingly important with the current density applied, to be finally generalized to all the processes related to H₂O transport at the H₂ electrode, while charge transfer is still disrupted.

We know that the appearance of the new phenomenon is characterized by the emergence of the positive contribution, assigned to a reactivation contribution, at the lowest frequencies. Moreover, a study conducted by Van Hassel et al. in SOFC mode showed that this kind of contribution can be

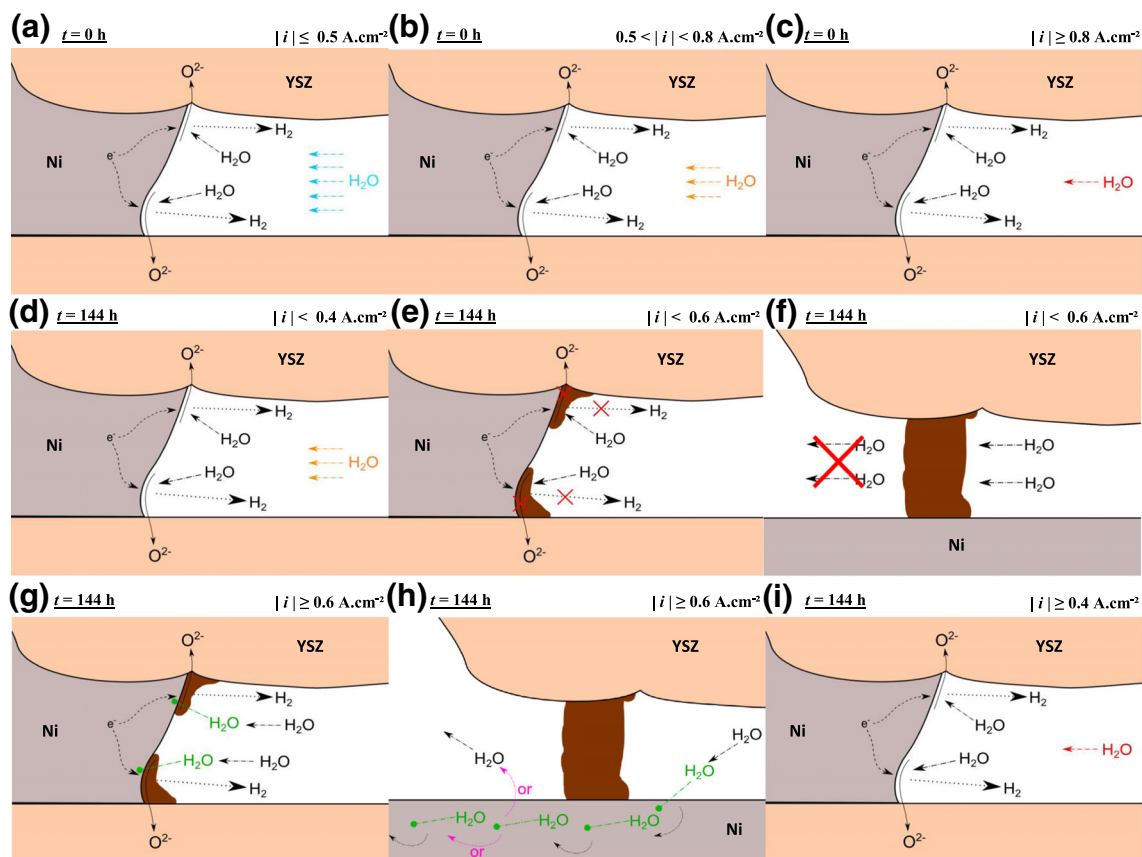
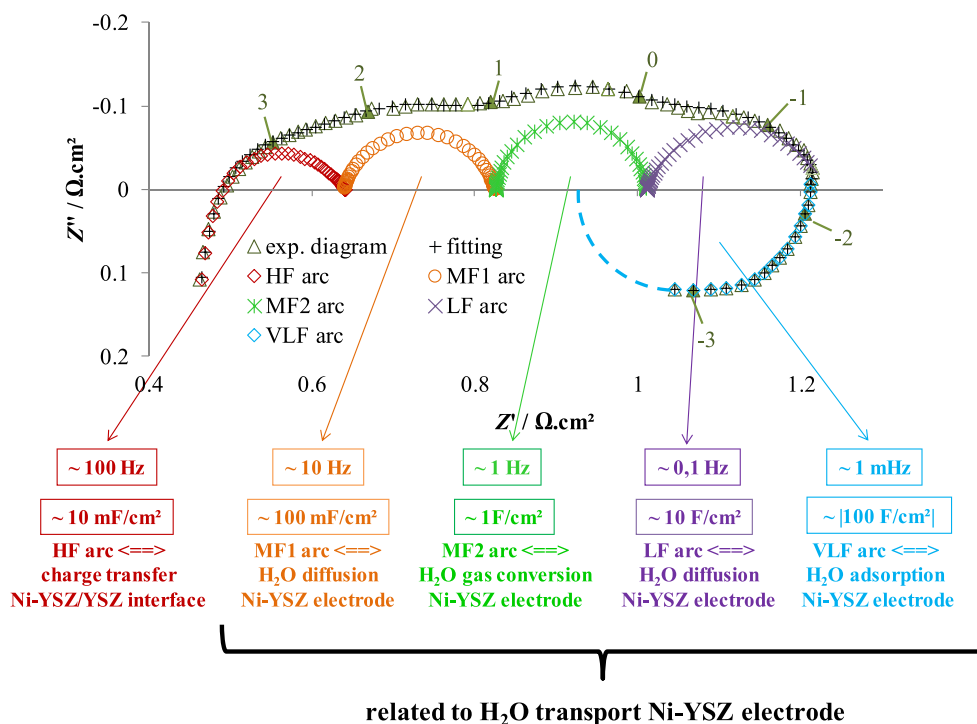


Fig. 10 Illustration of the mechanism explaining cell behavior while in use after impurity deposits containing Si at the root of the observed premature degradation. Initially ($t=0$ h), optimal functioning after cell activation (a), with no H₂O transport limitation for $|i| \leq 0.5$ A cm⁻²; partial limitation for $0.5 < |i| < 0.8$ A cm⁻² (b); important limitation by H₂O transport for $|i| \geq 0.8$ A cm⁻² (c). After premature degradation ($t=144$ h), partial limitation by H₂O transport from $|i| < 0.4$ A cm⁻² (d); presence of Si impurities at some TPBs prevents H₂O reduction reaction

(e); Si impurities disturb or even prevent H₂O crossing and so its transport toward TPBs mainly located at the Ni-YSZ/YSZ interface (f). For $|i| \geq 0.6$ A cm⁻², the applied current is sufficiently high to lead to a cell reactivation by H₂O adsorption (g) at TPBs polluted by Si impurities and/or H₂O shifting by surface adsorption/desorption (h) at Ni sites to “bypass” the pathways blocked by Si impurities. However, in the meantime, from $|i| = 0.4$ A cm⁻² (i), high limitation by H₂O transport which finally becomes predominant for cell functioning

Fig. 11 Illustration of the different impedance contributions identified in this study, with relaxation frequency and capacitance orders of magnitude for each contribution, as well as the associated phenomenon. Dashed lines refer to extrapolation of VLF arc to better visualize the last contribution



associated with O^{2-} adsorption phenomenon at the O_2 electrode/electrolyte interface [65, 66]. In this work, the cell is functioning in electrolysis mode, and the new phenomenon is related to the Ni-YSZ cathode. Therefore, this phenomenon might be associated with H_2O adsorption.

Mechanism of the premature degradation

As illustrated in Fig. 9, the premature degradation results from deposit of impurities containing Si at the H_2 electrode interface (surface and first dozens microns in the volume) and at the Ni-YSZ/YSZ interface. As a direct consequence, current collection is disrupted at the Ni-YSZ/current collector interface, and so charge transfer, but also H_2O transport. Thus, based on the analysis of the polarization curves and the impedance diagrams recorded in situ at different cell working times, and the SEM/EDX *post-mortem* characterization, a mechanism illustrated in Fig. 10 is proposed as follows to explain the cell behavior while in use further to the premature degradation:

- At $t = 0 \text{ h}$, the cell has a typical functioning, with H_2O supplied in excess for the lowest current densities applied (Fig. 10a), with less excess thereafter (Fig. 10b), before becoming limiting when the cell is used at the highest current densities applied (Fig. 10c);

- At $t = 144 \text{ h}$, because H_2O transport is (severely) limited by impurity deposits containing Si, the cell is functioning with a H_2O supply already diminished from the very lowest current densities applied (Fig. 10d). Si deposits affect H_2O transport in two ways: (i) H_2O cannot reach some TPBs contaminated

by these deposits (Fig. 10e), which prevents its reduction and so H_2 formation and (ii) H_2O crossing is disturbed or even prevented because of Si deposits (Fig. 10f), which leads to a H_2O depletion at the Ni-YSZ/YSZ interface from the lowest current densities.

This trend continues until a certain i value from which the applied current leads to the appearance of an H_2O adsorption phenomenon allowing H_2O reduction at the contaminated reaction sites (Fig. 10g) and H_2O transport in the blocked pathways (Fig. 10h). There is a reactivation of the cell resulting from this H_2O adsorption phenomenon. This trend continues until a certain i value above which transport limitation is significant (Fig. 10i), H_2O transport at the Ni-YSZ electrode becoming the predominant limiting phenomenon for the cell functioning. The cell behavior is then more the consequence of the cell under a too significant current demand than an effect of Si deposits. This mechanism, in fair agreement with the experimental data, can justify such an unexpected cell behavior not reported so far under electrolysis mode, to the best of our knowledge. Yet alternative phenomena such as adsorption of H_2O on YSZ surface remain also plausible.

Conclusions

To avoid a critical issue that represents H_2 leakage, glass sealing was used between the electrolysis cell holder and the support pieces. This beneficial effect was counterbalanced by the appearance of a premature degradation. This degradation was

characterized by a deformation of the i - U curve, several frequency shifts in the impedance diagrams as well as the appearance of a new impedance reactivation contribution at the lowest frequencies. This new impedance contribution has not been reported to date, to the best of our knowledge, in the case of a solid oxide cell working in electrolysis mode. The *post-mortem* cell analysis by SEM/EDX revealed the presence of Si, Al, Na, K, and Ca at the H₂ electrode interface (surface and first dozens microns in the volume) and at the Ni-YSZ/YSZ interface, by opposition to similar cells tested before without sealing of the pieces. Thus, this degradation was associated with Si deposition, including at the Ni/YSZ/H₂O TPBs, and the reactivation contribution characterized by ($[1-10 \text{ mHz}]$, $|100 \text{ F cm}^{-2}|$) to an H₂O adsorption phenomenon, including at these same TPBs. This contribution, which appears for the highest current densities applied, allows a renewal of the cell performance until limitation by H₂O transport becomes the predominant phenomenon governing the cell functioning. The evolution with time of the different resistive and capacitive contributions is consistent with the interpretation of the premature cell degradation. Analysis of the impedance diagrams, including by use of electrical equivalent circuits, allowed to clearly distinguish four to five contributions related to the functioning of the electrolysis cell as follows and illustrated in Fig. 11:

- HF part ($f_0 = [100-1000 \text{ Hz}]$; $C = 10 \text{ m F cm}^{-2}$) is associated with charge transfer at the Ni-YSZ/YSZ interface;
- MF1 part ($f_0 = 10 \text{ Hz}$; $C = 100 \text{ m F cm}^{-2}$) is related to an H₂O diffusion phenomenon at the H₂ electrode;
- MF2 part ($f_0 = 1 \text{ Hz}$; $C = 1 \text{ F cm}^{-2}$) is associated with H₂O gas conversion at the H₂ electrode;
- LF part ($f_0 = 0.1 \text{ Hz}$; $C = 10 \text{ F cm}^{-2}$) is also related to an H₂O diffusion phenomenon at the H₂ electrode; and
- VLF part ($f_0 = [1-10 \text{ mHz}]$; $C = |100 \text{ F cm}^{-2}|$) is associated with an H₂O adsorption phenomenon at the H₂ electrode.

Hence, this deeper analysis highlights that (i) all the dominant phenomena identified as driving cell operation in electrolysis mode are associated with the H₂ electrode and (ii) except charge transfer at the Ni-YSZ/YSZ interface, these phenomena are all related to H₂O transport at the H₂ electrode. Consequently, in order to enhance the performances of the system considered, further work should mainly focus on the H₂ electrode, and more particularly on the ways to optimize H₂O transport through the electrode. The observation of the premature degradation highlights the fact that the sealing process is a critical step that has to be reconsidered in future studies. Furthermore, this thorough electrochemical investigation based on chronopotentiometry and EIS sheds light onto how impurity deposit can dramatically affect the H₂ electrode and consequently the cell functioning.

Funding information This work is supported by the French Research National Agency (ANR) through *Hydrogène et piles à combustible* program (project FIDELHYO n°ANR-09-HPAC-005).

References

1. National Academy of Sciences, National Research Council (February 2004) The hydrogen economy: opportunities, costs, barriers. In: and R&D needs
2. Manage MN, Hodgson D, Milligan N, Simons SJR, Brett DJL (2011) *Int J Hydrog Energy* 36(10):5782–5796
3. Nechache A, Cassir M, Ringuedé A (2014) *J Power Sources* 258: 164–181
4. Fischer GW, Gels HB, Gross F, Liemert K, Rohr FJ (1978) *J Power Sources* 3(4):331–345
5. *Elektrochemische Prozesse* (1975) DECHEMA-Studie
6. Isenberg AO, Brecher LE (1970) Water vapor electrolysis at high temperatures, Westinghouse Electric Corp., Final Report, Project Fuel Cell, Rep. No. 57, Proc. First Int. Energy Agency Water Electrolysis Workshop. Brookhaven National Laboratory, Sept. 1975
7. Rohr FJ High temperature solid oxide fuel cells, Proc. Int. Energy Agency Workshop on Solid Electrolyte Fuel Cells. Brookhaven National Laboratory, May 1977
8. Isenberg AO (1981) *Solid State Ionics* 3/4:431–437
9. Maskalick NJ (1986) *Int J Hydrog Energy* 11(9):563–570
10. Barbi GB, Mari CM (1981) *Mater Chem* 6(1):35–54
11. Barbi GB, Mari CM (1982) *Solid State Ionics* 6(4):341–351
12. Barbi GB, Mari CM Paper presented at the 4th Int. Conf. on Solid State Ionics. Grenoble (4–8 July 1983)
13. Barbi GB, Mari CM (1988) *Solid State Ionics* 26(3):243–250
14. Barbi GB, Mari CM (1984) *Int J Hydrog Energy* 9(11):895–899
15. Dönitz W, Schmidberger R, Steinheil E (1980) *Int J Hydrog Energy* 5(1):55–63
16. Dönitz W, Schmidberger R (1982) *Int J Hydrog Energy* 7(4):321–330
17. Dönitz W, Erdle E (1985) *Int J Hydrog Energy* 10(5):291–295
18. Dönitz W, Dietrich G, Erdle E, Streicher R (1988) *Int J Hydrog Energy* 13(5):283–287
19. Chen K, Hyodo J, Ai N, Ishihara T, Jiang SP (2016) *Int J Hydrog Energy* 41(3):1419–1431
20. Hauch A, Jensen SH, Ramousse S, Mogensen M (2006) *J Electrochem Soc* 153(9):A1741–A1747
21. Jensen SH, Hauch A, Hendriksen PV, Mogensen M, Bonanos N, Jacobsen T (2007) *J Electrochem Soc* 154(12):B1325–B1330
22. Hauch A, Jensen SH, Mogensen M, Bilde-Sørensen JB (2007) *J Electrochem Soc* 154(7):A619–A626
23. Hauch A, Ebbesen SD, Jensen SH, Mogensen M (2008) *J Electrochem Soc* 155(11):B1184–B1193
24. Barfod R, Mogensen M, Klemenso T, Hagen A, Liu YL, Hendriksen PV (2007) *J Electrochem Soc* 154(4):B371–B378
25. Barfod R, Mogensen M, Klemenso T, Hagen A, Liu YL, Hendriksen PV (2005) In: Singhal SC, Mizusaki J (eds) *Solid Oxide Fuel Cells (SOFC IX)*, PV 2005–07, p 524. The Electrochemical Society Proceedings Series, Pennington, NJ
26. Ebbesen SD, Graves C, Hauch A, Jensen SH, Mogensen M (2010) *J Electrochem Soc* 157(10):B1419–B1429
27. Laguna-Bercero MA (2012) *J Power Sources* 203:4–16
28. Moçoteguy P, Brisse A (2013) *Int J Hydrog Energy* 38(36):15887–15902
29. Keane M, Fan H, Han M, Singh P (2014) *Int J Hydrog Energy* 39(33):18718–18726
30. Chen K, Ai N, Jiang SP (2014) *Int J Hydrog Energy* 39(20):10349–10358

31. Hjalmarsson P, Sun X, Liu YL, Chen M (2014) *J Power Sources* 262:316–322
32. Chen T, Liu M, Yuan C, Zhou Y, Ye X, Zhan Z, Xia C, Wang S (2015) *J Power Sources* 276:1–6
33. Knibbe R, Traulsen ML, Hauch A, Ebbesen SD, Mogensen M (2010) *J Electrochem Soc* 157(8):B1209–B1217
34. Pan Z, Liu Q, Lyu R, Li P, Chan SH (2018) *J Power Sources* 378: 571–578
35. Duboviks V, Maher RC, Kishimoto M, Cohen LF, Brandon NP, Offer GJ (2014) *Phys Chem Chem Phys* 16(26):13063–13068
36. Tao Y, Ebbesen SD, Mogensen MB (2014) *J Electrochem Soc* 161(3):F337–F343
37. Tao Y, Ebbesen SD, Zhang W, Mogensen MB (2014) *ChemCatChem* 6:1220–1224
38. Skafta TL, Blennow P, Hjelm J, Graves C (2018) *J Power Sources* 373:54–60
39. Duboviks V, Lomberg M, Maher RC, Cohen LF, Brandon NP, Offer GJ (2015) *J Power Sources* 293:912–921
40. Zheng Y, Li Q, Chen T, Wu W, Xu C, Wang WG (2015) *Int J Hydrog Energy* 40(6):2460–2472
41. Kim SJ, Kim KJ, Choi GM (2015) *J Power Sources* 284:617–622
42. Hjalmarsson P, Sun X, Liu YL, Chen M (2013) *J Power Sources* 223:349–357
43. Nechache A, Mansuy A, Petitjean M, Mougín J, Mauvy F, Boukamp BA, Cassir M, Ringuedé A (2016) *Electrochim Acta* 210:596–605
44. Brisse A, Schefold J, Zahid M (2008) *Int J Hydrog Energy* 33(20): 5375–5382
45. Leonide A, Sonn V, Weber A, Ivers-Tiffée E (2008) *J Electrochem Soc* 155(1):B36–B41
46. Dasari HP, Park SY, Kim J, Lee JH, Kim BK, Je HJ, Lee HW, Yoon KJ (2013) *J Power Sources* 240:721–728
47. Fan H, Keane M, Singh P, Han M (2014) *J Power Sources* 268:634–639
48. Schefold J, Brisse A, Zahid M (2009) *J Electrochem Soc* 156(8): B897–B904
49. Wang W, Huang Y, Jung S, Vohs JM, Gorte RJ (2006) *J Electrochem Soc* 153(11):A2066–A2070
50. Hanifi AR, Laguna-Bercero MA, Etsell TH, Sarkar P (2014) *Int J Hydrog Energy* 39(15):8002–8008
51. Laguna-Bercero MA, Campana R, Larrea A, Kilner JA, Orera VM (2011) *J Power Sources* 196(21):8942–8947
52. Jiang SP, Badwal SPS (1999) *Solid State Ionics* 123(1–4):209–224
53. Laguna-Bercero MA, Kilner JA, Skinner SJ (2010) *Chem Mater* 22(3):1134–1141
54. Chen S, Xie K, Dong D, Li H, Qin Q, Zhang Y, Wu Y (2015) *J Power Sources* 274:718–729
55. Anderson JC, Leaver KD, Rawlings RD, Alexander JM (1990) *Materials science*. Chapman & Hall, New York
56. Doremus RH (1973) *Glass science*. John Wiley & Sons, New York
57. Holland L (1964) *The properties of glass surface*. Chapman and Hall, London
58. Butler EP, Drennan J (1982) *J Am Ceram Soc* 65(10):474–478
59. Jewell JM, Spess MS, Shelby JE (1990) *J Am Ceram Soc* 73(1): 132–135
60. Jewell JM, Shelby JE (1990) *J Cryst Growth* 73:1446
61. Shelby JE, Mcvay GL (1976) *J Non-Cryst Solids* 20(3):439–449
62. Mansuy A (2012) PhD Thesis, Université Bordeaux 1
63. Nechache A (2014) PhD thesis, Université Pierre et Marie Curie, Paris
64. Virkar AV (2007) *J Power Sources* 172(2):713–724
65. van Hassel BA, Boukamp BA, Burggraaf AJ (1991) *Solid State Ionics* 48:139–154
66. van Hassel BA, Boukamp BA, Burggraaf AJ (1991) *Solid State Ionics* 48:155–171